Article

Optimization of Electron and Hole Transport Layer to Model A Lead-Free Inorganic $Cs_3Bi_2I_9$ Based Perovskite Solar Cell and Investigating the Effects of Different Attributes on Device Performance

Arnob Das[a,*], Sujan Banik[a], Barun K. Das[a], Nurul Islam[a]

[a] [a]Department of Mechanical Engineering, Rajshahi University of Engineering and Technology, Rajshahi-6204, Bangladesh

* Correspondence: arnobarjun@gmail.com

Abstract: Research on the lead halide-based perovskite solar cells have obtained considerable interest in photovoltaic industry owing to their higher efficiency, easy manufacturing, light-weight and low cost. However, these lead halide-based solar cells are not suitable to manufacture commercially because of the toxicity of lead-based materials. In this context, a lead-free perovskite, cesium-bismuth iodide ($Cs_3Bi_2I_9$) is considered as a potential alternative to the lead halide-based cell due to their non-toxicity and stability, but this perovskite cannot be matched with random hole transport layer (HTL) and electron transport layer (ETL) materials compared to lead halide-based perovskite because of their crystal structure and band gap. Therefore, in this study, performance comparison of different ideal HTL and ETL materials for $Cs_3Bi_2I_9$ perovskite layer were studied using SCAPS-1D device simulation on the basis of open circuit voltage, short circuit current, power conversion efficiency (PCE) and fill factor (FF) as well as several novel PSC configuration model were designed that can direct for further experimental research for PSC device commercialization. Results from this investigation reveals that the maximum efficiency of 20.96% is obtained for the configuration ITO/WS_2/$Cs_3Bi_2I_9$/NiO/Au with optimized parameters such as thickness 400 nm, band gap 2.1eV, absorber layer defect density 10^{12} cm^{-3}, donor density of ETL 10^{18} cm^{-3} and the acceptor density of HTL 10^{20} cm^{-3}.

Graphical abstract

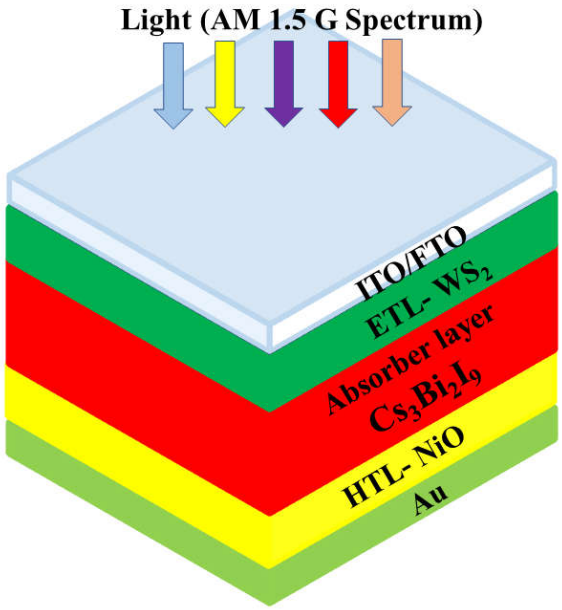

 doi:10.20944/preprints202305.1729.v1

Keywords: Perovskite solar cell; Lead-free $Cs_3Bi_2I_9$; HTL; ETL; Fill factor; PCE

1. Introduction

The consumption of power and energy is increasing with accelerated commercialization and industrialization[1]. The continuous utilization of conventional fuels such as natural gas, oils, hydrocarbon gas liquids, fossil fuels and the severe environmental effect for using these materials raises serious concerns about the research of alternate energy resources [2–4]. To replace the non-renewable energy resources and to fulfill the increasing energy demand in an environment friendly way, proper utilization of renewable energy sources is badly needed [5,6]. Solar energy stands out as a viable renewable energy resource among different potential renewable sources such as wind energy, geothermal energy, hydro power, ocean energy, bioenergy and tidal energy. In recent years, solar cell production is expanding significantly today as the cost of solar cells lowers. However, in order to compete with fossil fuels and transform into a substantial energy source, the expenses of solar cells must be minimized. Considerable initiatives have been taken to create novel cell materials, and recently, a new generation of perovskite solar cells (PSCs) has been established that shows satisfactory performances to go for commercialization. The PSC will most likely have a huge impact on the future solar cell industry due to the low cost of raw materials and the simple manufacturing method, and this kind of cell may also be competitive with natural gas [7].

The solar research field have been recently captured by organic-inorganic PSCs due to having exceptional and excellent properties such as high absorptivity, low atomic energy, improved dielectric constant, favorable deposition by solution processing technique, high electron mobility, high hole mobility, suitable with low manufacturing cost and low-temperature deposition than conventional silicon-based solar cells [8,9]. The efficiency and stability of perovskites solar cells show tremendous improvement such as in just 10 years perovskite solar cells developed from unstable 3% efficiency to stable 32% efficiency [10] and this improvement shows the potentiality of perovskite solar cells for which these solar cells have raised as strong competitor in the photovoltaic industry [11–13].

Thin-film PSC technology has improved due to the ease fabrication, energy gap adjustability, and the photon conversion efficiency (PCE) above 30% of lead (Pb)-compounded organic inorganic halide PSCs [14]. Although these achievements, the existence of emerging contaminants (Pb) that causes toxicity is the fundamental issues in the applications of lead-based PSCs and this problem is still a significant barrier to commercialization of PSCs [15]. Additionally, the perovskite layer's organic components contribute to the solar cell's instability. Similarly, the presence of organic elements in the perovskite layer causes instability of the solar cell. Therefore, lead based organic halide perovskite solar cells are not suitable and preferable for industrial application and commercialization. To eliminate the toxicity researchers have carried out experiments to develop lead-free perovskite material and to minimize instability utilizing inorganic materials have gathered attractive attention which can replace organic materials [16–18]. Ahmad et al. simulated a $Cs_3Bi_2I_9$ based 2D PSC device where they employed TiO_2 as ETL material and Spiro-MeOTAD as HTL material with gold as back contact[19]. Their simulation results revealed that their PSC device could gain an efficiency of 11.54% and their experimental results showed 1.66% efficiency for the similar configuration. Researchers are also working for stabilizing experimented PSC devices against several influencing natural factors such as moisture, temperature and dust. Hamukwaya et al.[20] experimented to investigate the performance after adding KI as additive with $Cs_3Bi_2I_9$ perovskite layer. This mixing of KI caused the highest efficiency as 2.81% the $Cs_3Bi_2I_9$ perovskite layer highly stabilizes the resultant PSC device against humidity to the extent that it maintains 98% of the initial PCE after 90 days, which is suitable for solar cell applications.

Homo-valent component such as Ge^{2+} and Sn^{2+} can be a potential choice which can eliminate toxicity; however, these components decrease the stability of PSCs when it performs at ambient temperature [21–23]. For alternation of such materials different hetero-valent materials are tested in lab-based experiments to investigate their suitability and stability for using in perovskite layers and among those materials Bi^{3+}

Preprints (www.preprints.org) | NOT PEER-REVIEWED | Posted: 25 May 2023 doi:10.20944/preprints202305.1729.v1

and Sb^{3+} which have stable +3 oxidation phase have gathered much attention[24]. Bi^{3+} have good optoelectronic properties as Pb^{2+} due to ionic radius and electronic structure similarities of these materials. Among different Bi halide-based materials $Cs_2Bi_2I_9$ achieved the greatest interest due to its higher PCE and more stability than other Bi based perovskite materials [25,26]. Summary of different works on the PSC performance analysis are listed in **Table 1**.

$Cs_3Bi_2I_9$ is a hybrid organic-inorganic perovskite material that has gained attention in the field of photovoltaics as a potential absorber layer in solar cells. This material has a range of advantages that make it an attractive candidate for this application. One of the significant advantages of $Cs_3Bi_2I_9$ is its high absorption coefficient. This characteristic enables it to absorb light effectively across a broad range of the solar spectrum, which is essential for the efficient operation of solar cells. The high absorption coefficient of $Cs_3Bi_2I_9$ is comparable to other well-known perovskite absorbers like $MAPbI_3$ (methylammonium lead iodide). Another advantage of $Cs_3Bi_2I_9$ is its high stability. Many perovskite materials are known to be unstable under ambient conditions, which can limit their practical applications. However, Cs3Bi2I9 has been shown to be highly stable under various environmental conditions, including humidity, light, and heat. This stability makes it an attractive option for use in real-world applications where stability is crucial. $Cs_3Bi_2I_9$ also has high carrier mobility, which is a desirable property for efficient charge transport and collection in photovoltaic devices. Furthermore, this material has a direct bandgap, which is crucial for efficient light absorption and conversion into electrical energy in photovoltaic devices[24].

In this study, the simulation has been carried out in two steps, where the first step consists of comparison of suitable ETL and HTL materials with $Cs_3Bi_2I_9$ absorber layer to find out the best configuration for which higher performance has been observed. In second step, the selected model has been optimized for improving its performance parameters such as J_{sc}, V_{oc}, PCE and FF. To achieve the optimized system, around 45 models with different ETL and HTL materials have been performed. In this process, a best performance for ITO/WS_2/$Cs_3Bi_2I_9$/NiO/Au has been attained. For further improvement of this configuration, optimization of various adjustable attributes such as thickness and bandgap of absorber layer, defect density of absorber layer and charge carrier density of HTL and ETL materials has been done. After tuning input attributes, 20.96% of PCE has been obtained for this model.

Table 1: Literature review on recent experimental perovskite-based solar cells performance.

Device structure	Year	PCE(%)	V_{OC}(V)	J_{SC}(mA/cm²)	FF(%)	Ref
Au/spiro-OMeTAD/ FTO/TiO2	2022	12.54	1.32	13.13	72.01	[27]
HTL/back contact /$MAPbBr_3$/SnO_2/ FTO	2021	25.40	1.19	25.09	84	[28]
Ag/BCP/PCBM/($Cs_{0.05}$(FA5/MAI)-$_{0.95}$Pb($I_{0.9}Br_{0.1}$)$_3$)/PTAA/TTO/Glass	2021	23	1.16	24	82	[29]
Cu/BCP/ITUC_{60}/$Cs_{0.05}$($FA_{0.92}MA_{0.08}$)$_{0.95}$Pb($I_{0.92}Br_{0.08}$)$_3$/ PTAA/ITO	2020	22.30	1.71	24.10	81	[30]
Au/ Spiro-OMeTAD/$CsSn_{0.5}Ge_{0.5}I_3$/PCBM/FTO	2019	7.11	0.63	18.61	60.6	[31]
ITO/NiO_x/$FASnI_3$/PCBM/Ag	2018	6.70	0.60	17.53	65	[32]
Ag/PCBM/$MASn_{0.6}Pb_{0.4}I_{3-x}Br_x$/PEDOT:PSS/ITO	2017	12.10	0.78	20.65	75	[33]
Au/Spiro-OMeTAD/$Cs_{0.16}FA_{0.84}Pb(I_{0.88}Br_{0.12})_3$/$SnO_2$/FTO	2016	18	1.02	22.40	78	[34]
Ag/BCP/PCBM/0.15 mol% Al_3+-doped$CH_3NH_3PbI_3$/ Poly-TPD/FTO	2016	19.10	1.01	22.40	78	[35]
Au/spiro-OMeTAD /$MASnI_3$/ ZnO/ITO	2015	7.66	0.97	11.10	66	[36]
Au/SpiroOMeTAD + LiTFSI + tBP /$MASnI_3$/ m-TiO_2/ TiO_2	2014	6.40	0.88	16.80	42	[37]

Preprints (www.preprints.org) | NOT PEER-REVIEWED | Posted: 25 May 2023 doi:10.20944/preprints202305.1729.v1

2. Model development and perovskite solar cell structure

2.1. Numerical modeling

In order to construct any form of a practical solar cell, numerical models have become a crucial tool. Perovskite solar cells' numerical modeling is a crucial technique for evaluating the validity of the proposed physical reasons and predicting the impact of physical modifications on cell performance [38]. Numerical modeling is required because perovskite solar cells are so complicated in their behavior [39].

Numerical simulation software offers useful information to select materials before experiment and commercialization. The One Dimension Solar Cell Capacitance Simulator (SCAPS-1D) program which is created by Burgelman et al. [40] can be used to do the numerical calculations of PSCs [41]. SCAPS-1D software solves the charge carrier continuity Equations such as hole continuity Equation 1 and electron continuity Equation 2, the semiconductor Poisson Equation 3 in one direction, total charge transport Equation 4, electron transport Equation 5, hole transport Equation 6 and optical absorption coefficient Equation 7.

$$\frac{dn_p}{dt} = G_n - \frac{n_p - n_{p0}}{\tau_n} + n_p\mu_n\frac{d\xi}{dx} + \mu_n\xi\frac{dn_p}{ds} + D_n\frac{d^2n_p}{dx^2} \quad (1)$$

$$\frac{dn_n}{dt} = G_p - \frac{p_n - p_{n0}}{\tau_p} + p_n\mu_p\frac{d\xi}{dx} + \mu_p\xi\frac{dn_n}{ds} + D_p\frac{d^2p_n}{dx^2} \quad (2)$$

$$\frac{d^2\emptyset(x)}{dx^2} = \frac{q}{\epsilon_o\epsilon_r}\left(p(x) - n(x) + N_D - N_A + -0.3\rho_p - -0.3\rho_n\right) \quad (3)$$

$$J = J_n + J_p \quad (4)$$

$$J_n = D_n\frac{dn}{dx} + \mu_n n\frac{d\phi}{dx} \quad (5)$$

$$J_p = D_p\frac{dp}{dx} + \mu_p p\frac{d\phi}{dx} \quad (6)$$

$$\alpha(\lambda) = \left(A + \frac{B}{hv}\right)\sqrt{hv - E_g} \quad (7)$$

where, ξ is the electric field, q denotes electrical charge whose typical value is considered as 1.602×10^{-19}C, ϵ_o is the vacuum absolute permittivity and ϵ_r is the semiconductor relative permittivity, N_D and N_A represent donor doping density and acceptor doping density respectively, p(x) and n(x) are carrier density of hole and electron, -0.3ρ_p is the defect density of hole and -0.3ρ_n is the defect density of electron, G_n and G_p indicates electron generation rate and hole generation rate respectively, J_n and J_p are current density and hole current density of electron, respectively, μ_n and μ_p are electron and hole mobilities, τ_n and τ_p represents lifetime of electrons and holes respectively, D_p and D_n represents diffusion coefficient of free hole and electron. v represents optical frequency, A and B depicts arbitrary

Preprints (www.preprints.org) | NOT PEER-REVIEWED | Posted: 25 May 2023 doi:10.20944/preprints202305.1729.v1

constant while E_g represents bandgap, h represents plank constant and $\alpha(\lambda)$ depicts absorption coefficient. More information about these equations can be learned from somewhere [42–46].

2.2. PSC structure and material charateristics

2.2.1. PSC structure

The device structure in this paper is Au/HTL/absorber layer/ETL/ITO/glass, where Au is employed as back contact having work function of 5.1eV and $Cs_3Bi_2I_9$ is applied as absorber or perovskite layer. The simulation is carried out with different ETLs and HTLs to obtain a novel optimized configuration. The ETLs that are simulated in this study include TiO_2, PCBM, WS_2, IGZO and C60 whereas CuO, Cu_2O, PEDOT:PSS, P3HT, CuSCN, $CuSbS_2$, NiO, Spiro-OMeTAD and CuI are applied as hole transport layer material.

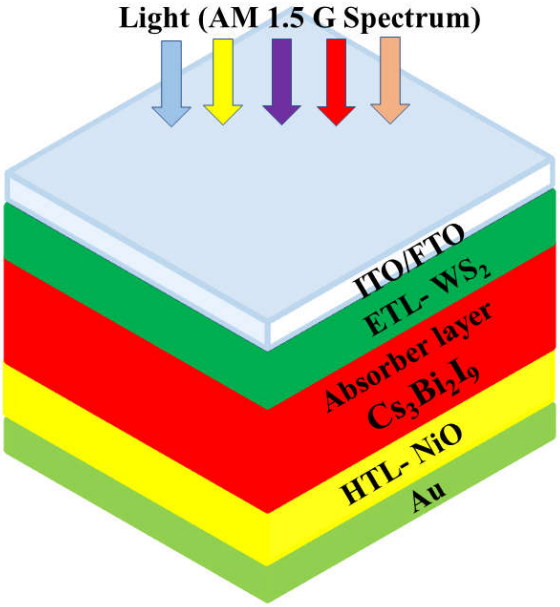

Figure 1: Model of a perovskite-based solar cell with different layers.

Figure ***1*** shows a typical model of PSC with different layers such as ITO, ETL, absorber layer and HTL.

Preprints (www.preprints.org) | NOT PEER-REVIEWED | Posted: 25 May 2023 doi:10.20944/preprints202305.1729.v1

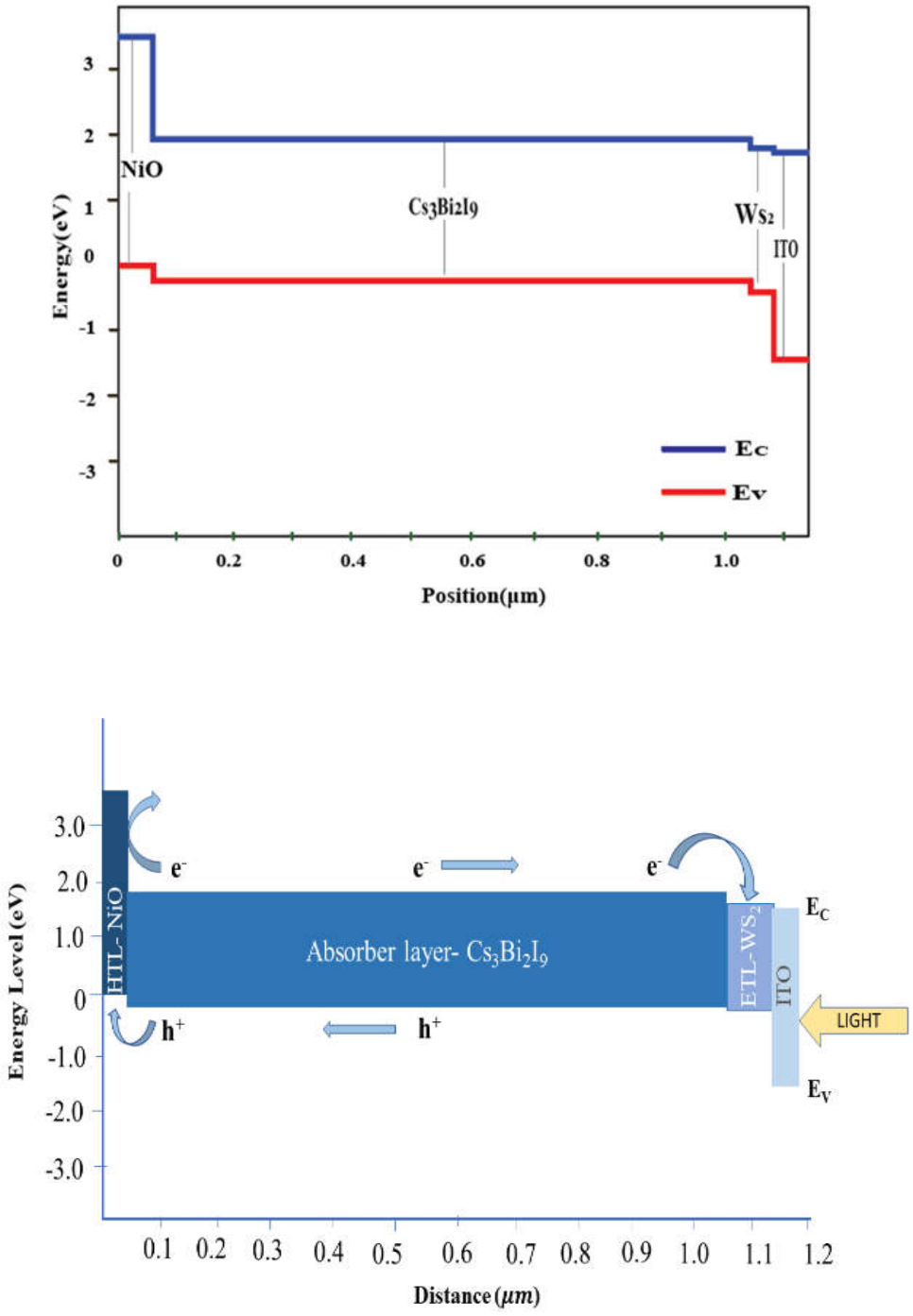

Figure 2: Energy band diagram for the selected configuration in this study.

The band diagram of our selected configuration is showed in **Figure 2**, from where it can be seen that the blue curve depicts the conduction band line and red curve shows the valence band line.

Preprints (www.preprints.org) | NOT PEER-REVIEWED | Posted: 25 May 2023 doi:10.20944/preprints202305.1729.v1

2.2.2. Physical input parameters and methodology

The AM1.5 illumination spectrum is used by default in this study. The incident light power (Ps) and temperature are fixed at 1000 W/m² and 300 K, respectively. In every layer, the thermal velocities of the electrons and holes are fixed at 10^7 cm/s. The absorption co-efficient (α) of ETL and HTL layers are determined in SCAPS-1D through Equation 8 [47], like in many works on PSCs,

$$\alpha = A_a\sqrt{(hv - E_g)} \quad (8)$$

where, A_a is a layer-dependent pre-factor in the simulation. The application of interface defects has schemed the design more realistic and assisted to predict the experimental behavior of the solar cell model.

Table 2: Input attributes for perovskite material, different electron transport layer (ETL) materials and ITO.

Parameter	$Cs_3Bi_2I_9$ [48]	PCBM[49,50]	TiO_2 [51–53]	WS_2 [54]	IGZO [49]	C60 [55]	ITO [56]
Electron affinity, X (eV)	3.40	3.90	4.26	3.95	4	3.90	4.1
Relative permittivity (ε_r)	9.68	4	100	13.60	9	4.20	10
Thickness(nm)	1000	30	30	100	30	50	60
Bandgap, E_g (eV)	2.1	2	3.20	1.80	3.50	1.70	3.6
State density of conduction band, N_C (1/cm³)	4.98×10^{19}	1×10^{21}	2×10^{18}	10^7	5×10^{18}	8.0×10^{19}	2.2×10^{18}
State density of valence band, N_V (1/cm³)	2.11×10^{19}	2×10^{20}	1.8×10^{19}	10^7	5×10^{18}	8.0×10^{19}	1.8×10^{19}
AL defect density, N_t (1/cm³)	10^{14}	1×10^{14}	1×10^{15}	10^{15}	1×10^{15}	1×10^{14}	-
Mobility of electron, μ_n(cm²/Vs)	10^7	1×10^{-2}	2×10^4	100	15	8.0×10^{-2}	10^7
Mobility of hole, μ_p(cm²/Vs)	10^7	1×10^{-2}	1×10^3	100	0.20	3.5×10^{-3}	10^7
AD, N_A(1/cm³)	10^{19}	-	-	-	-	-	-
DD, N_D(1/cm³)	10^{19}	1×10^{20}	6×10^{19}	10^{18}	1×10^{17}	2.6×10^{17}	10^{19}

Preprints (www.preprints.org) | NOT PEER-REVIEWED | Posted: 25 May 2023 doi:10.20944/preprints202305.1729.v1

Table 3: Input attributes for different hole transport layer (HTL) materials.

Parameter	NiO [50]	CuO [57]	Cu_2O [58]	PEDOT [59]	P3HT [58]	CuSCN [58]	CuI [60–63]	Spiro-OMeTAD [64]	$CuSbS_2$ [65–67]
Relative permittivity (ε_r)	11.75	18.1	7.1	3	3	10	6.5	3	14.6
Bandgap, E_g(eV)	3.6	31.5	2.17	3.6	1.7	3.4	2.98	2.9	1.58
Electron affinity, X(eV)	2.1	4.07	3.2	1.57	3.5	2.1	2.1	2.2	4.2
Thickness(nm)	50	50	50	50	50	50	50	350	50
AL defect density, N_t ($1/cm^3$)	1×10^8	1×10^{13}	1×10^{13}	1×10^{14}	1×10^{14}	1×10^8	1×10^{15}	1×10^{13}	1×10^{18}
State density of conduction band, N_C ($1/cm^3$)	2.5×10^{20}	2.2×10^{19}	2.5×10^{20}	2.2×10^{18}	2×10^{18}	2.5×10^{18}	2.8×10^{19}	2.5×10^{18}	2×10^{18}
State density of valence band, N_V ($1/cm^3$)	2.5×10^{20}	5.5×10^{20}	2.5×10^{20}	1.8×10^{19}	2×10^{19}	1.8×10^{19}	1×10^{19}	1.8×10^{19}	1×10^{18}
Mobility of electron, μ_n (cm^2/Vs)	1×10^{-3}	100	200	100	1.8×10^{-3}	2×10^{-4}	1.69×10^{-4}	2×10^{-4}	49
Mobility of hole, μ_p(cm^2/Vs)	1×10^{-3}	0.1	8600	4	1.8×10^{-2}	2×10^{-4}	1.69×10^{-4}	2×10^{-4}	49
AD, N_A($1/cm^3$)	1×10^{19}	1×10^{15}	1×10^{19}	2×10^{19}	1×10^{18}	1×10^{17}	1×10^{18}	1×10^{17}	1×10^{18}
DD, N_D($1/cm^3$)	-	-	-	-	-	-	-	-	-

Preprints (www.preprints.org) | NOT PEER-REVIEWED | Posted: 25 May 2023 doi:10.20944/preprints202305.1729.v1

PSC device investigation has been carried out in two different steps where the first step includes building up a PSC device configuration with suitable HTL and ETL for $Cs_3Bi_2I_9$ absorber layer. Different input attributes for nine HTL materials have been listed in **Table 2** and input parameters for five ETL materials has been listed in **Table 3.** With these various ETL and HTL materials 45 different configurations have been simulated. After scrutinized comparison, it was found that when WS_2 as ETL and NiO as HTL were applied as charge transporting layers then the configuration (ITO/WS_2/$Cs_3Bi_2I_9$/NiO/Au) have showed best results with higher performance parameters. In second stage, the selected model (ITO/WS_2/$Cs_3Bi_2I_9$/NiO/Au) has been optimized by tuning bandgap and thickness of absorber layer, defect density of absorber layer and carrier density of ETL and HTL.

3. Results and discussion

3.1. Optimization of ETL and HTL

In this study, $Cs_3Bi_2I_9$ was selected as absorber layer due to its non-toxicity and better optoelectronic parameter, however it's hard enough to match this absorber layer with appropriate ETL and HTL due to band structure of $Cs_3Bi_2I_9$. To obtain the best performance, simulation of the configuration (ITO/ETL/$Cs_3Bi_2I_9$/HTL/Au) for five different ETL materials and nine different HTL materials have been carried out.

Figure 3 shows performance parameters of different PSC configurations for different HTLs where PCBM and $Cs_3Bi_2I_9$ were applied as ETL and absorber layer respectively. In a similar way, **Figure *4*** shows performance parameters for WS_2 ETL, **Figure *5*** shows comparison for IGZO ETL, **Figure *6*** reveals performance comparison for C60 ETL as well as comparison for TiO_2 ETL can be observed in **Figure 7**.

After scrutinized comparison, it can be observed from these figures that when NiO and WS_2 were applied as HTL and ETL, respectively, the configuration ITO/WS_2/$Cs_3Bi_2I_9$/NiO/Au shows best performance characteristics. The optimized characteristics are given in **From Figures 4-7,** it can be observed that the maximum 20.25% PCE can be achieved when WS2 and NiO were employed as ETL and HTL material respectively with Cs3Bi2I9 perovskite layer. Cu2O also showed extraordinary performance with WS2 ETL and Cs3Bi2I9 absorber layer. However, as the configuration ITO/WS2/Cs3Bi2I9/NiO/Au shows best performance so further optimization was carried out for this model.

 doi:10.20944/preprints202305.1729.v1

Table 4 for which improved performance characteristics were obtained. From **Figures 4-7**, it can be observed that the maximum 20.25% PCE can be achieved when WS_2 and NiO were employed as ETL and HTL material respectively with $Cs_3Bi_2I_9$ perovskite layer. Cu_2O also showed extraordinary performance with WS_2 ETL and $Cs_3Bi_2I_9$ absorber layer. However, as the configuration ITO/WS_2/$Cs_3Bi_2I_9$/NiO/Au shows best performance so further optimization was carried out for this model.

Preprints (www.preprints.org) | NOT PEER-REVIEWED | Posted: 25 May 2023 doi:10.20944/preprints202305.1729.v1

Table 4: Optimized input attributes for the selected configuration in this study.

Parameters	ITO	WS_2	$Cs_3Bi_2I_9$	NiO
Electron affinity (eV)	4.1	3.95	3.4	2.1
Bandgap (eV)	3.6	1.8	**2.10**	3.6
Thickness (nm)	60	100	**400**	150
Dielectric permittivity (relative)	10	13.6	9.68	11.75
Thermal velocity of hole (cm/s)	10^7	10^7	10^7	10^7
Mobility of electron (cm^2/Vs)	50	100	4.3	10^{-3}
CB effective density of states (cm^{-3})	2.2×10^{18}	2×10^{18}	4.98×10^{19}	2.5×10^{20}
VB effective density of states (cm^{-3})	1.8×10^{19}	2×10^{18}	2.11×10^{19}	2.5×10^{20}
Thermal velocity of electron (cm/s)	10^7	2×10^5	10^7	10^7
Mobility of hole (cm^2/Vs)	75	100	1.7	10^{-3}
Shallow uniform DD, N_D (cm^{-3})	10^{19}	$\mathbf{10^{18}}$	10^{19}	-
Shallow uniform AD, N_A (cm^{-3})	-	-	10^{19}	$\mathbf{1\times10^{20}}$
Defect density of AL, N_t (cm^{-3})	-	10^{13}	$\mathbf{10^{12}}$	1×10^{14}

Note: The bold attributes depicts the optimized input paramters.

Preprints (www.preprints.org) | NOT PEER-REVIEWED | Posted: 25 May 2023 doi:10.20944/preprints202305.1729.v1

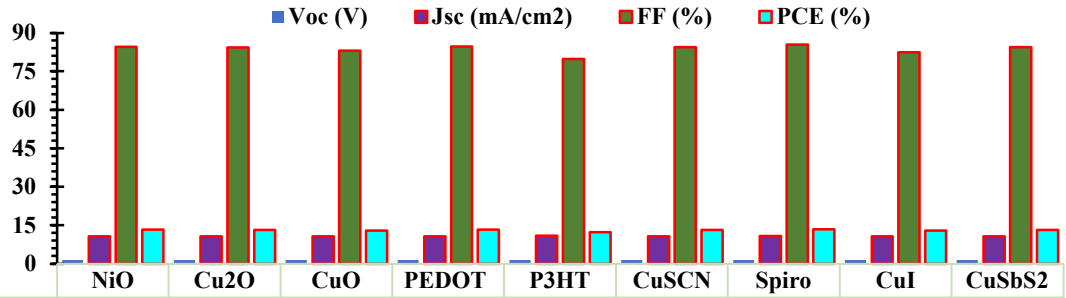

	NiO	Cu2O	CuO	PEDOT	P3HT	CuSCN	Spiro	CuI	CuSbS2
Voc (V)	1.463	1.459	1.478	1.4628	1.405	1.463	1.4585	1.4623	1.461
Jsc (mA/cm2)	10.698	10.706	10.694	10.699	10.89	10.698	10.74	10.699	10.698
FF (%)	84.53	84.27	83.04	84.58	79.76	84.38	85.45	82.4	84.33
PCE (%)	13.23	13.17	12.86	13.24	12.22	13.21	13.4	12.89	13.18

Figure 3: Performance parameters for different HTLs with PCBM ETL and Cs3Bi2I9 absorber layer.

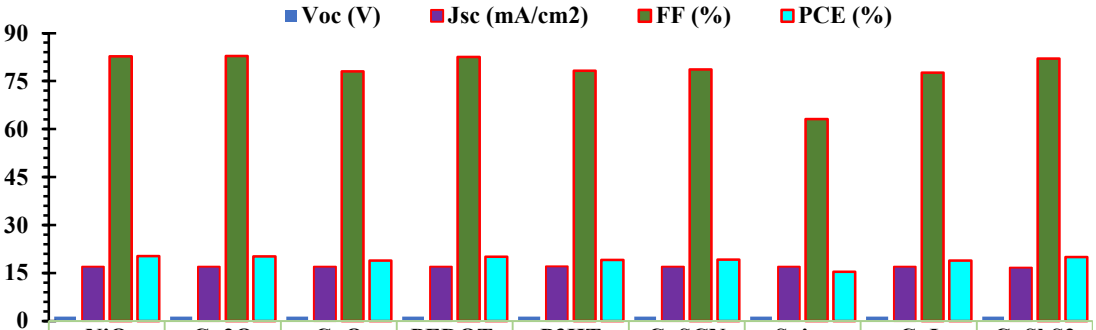

	NiO	Cu2O	CuO	PEDOT	P3HT	CuSCN	Spiro	CuI	CuSbS2
Voc (V)	1.4356	1.4356	1.4298	1.4355	1.4287	1.4358	1.4348	1.435	1.4349
Jsc (mA/cm2)	16.97	16.97	16.97	16.97	17.05	16.97	16.96	16.97	16.67
FF (%)	82.7	82.81	78.07	82.57	78.21	78.64	63.16	77.64	82.03
PCE (%)	20.25	20.18	18.94	20.12	19.05	19.16	15.38	18.88	19.98

Figure 4: Performance parameters for different HTLs with WS_2 ETL and Cs3Bi2I9 absorber layer.

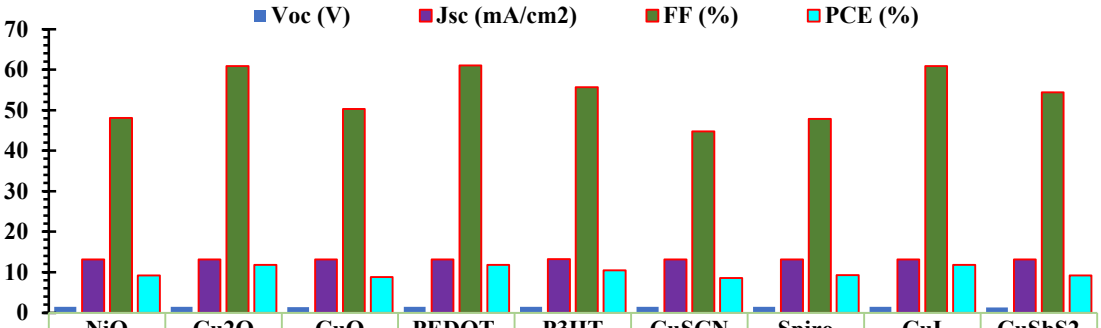

	NiO	Cu2O	CuO	PEDOT	P3HT	CuSCN	Spiro	CuI	CuSbS2
Voc (V)	1.447	1.466	1.331	1.468	1.418	1.448	1.466	1.468	1.28
Jsc (mA/cm2)	13.16	13.17	13.12	13.17	13.21	13.16	13.17	13.17	13.17
FF (%)	48.09	60.89	50.27	60.99	55.66	44.72	47.8	60.86	54.38
PCE (%)	9.16	11.77	8.78	11.79	10.43	8.53	9.23	11.77	9.17

Figure 5: Performance parameters for different HTLs with IGZO ETL and Cs3Bi2I9 absorber layer.

Preprints (www.preprints.org) | NOT PEER-REVIEWED | Posted: 25 May 2023 doi:10.20944/preprints202305.1729.v1

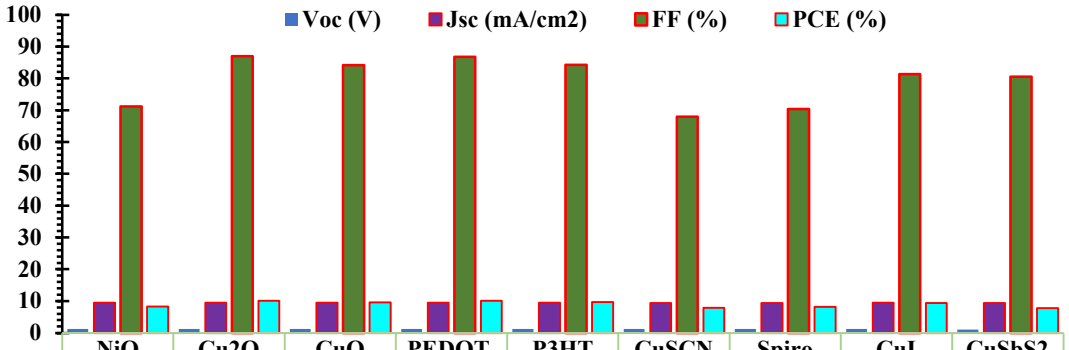

	NiO	Cu2O	CuO	PEDOT	P3HT	CuSCN	Spiro	CuI	CuSbS2
Voc (V)	1.225	1.226	1.21	1.226	1.21	1.225	1.225	1.225	1.03
Jsc (mA/cm2)	9.436	9.458	9.451	9.448	9.516	9.43	9.416	9.432	9.43
FF (%)	71.13	86.95	84.14	86.79	84.21	68	70.4	81.38	80.5
PCE (%)	8.23	10.08	9.63	10.06	9.69	7.86	8.13	9.41	7.77

Figure 6: Performance parameters for different HTLs with C60 ETL and Cs3Bi2I9 absorber layer.

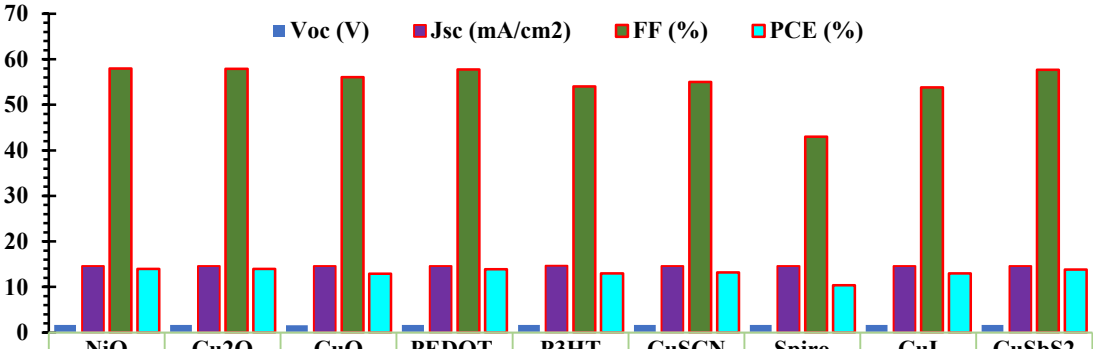

	NiO	Cu2O	CuO	PEDOT	P3HT	CuSCN	Spiro	CuI	CuSbS2
Voc (V)	1.65	1.65	1.57	1.65	1.64	1.65	1.65	1.65	1.64
Jsc (mA/cm2)	14.571	14.572	14.572	14.573	14.69	14.571	14.576	14.574	14.571
FF (%)	57.96	57.92	56.11	57.76	54.04	55	42.97	53.81	57.67
PCE (%)	13.96	13.96	12.89	13.91	13.01	13.22	10.34	12.95	13.82

Figure 7: Performance parameters for different HTLs with TiO_2 ETL and Cs3Bi2I9 absorber layer.

3.2. Effect of absorber layer thickness

The light-absorbing layer thickness has a great impact on the performance of PSCs. The layer needs an optimized thickness for the collection of solar radiation basically to collect photons and facilitates the electron and hole pair generation. The photon absorption density drops hence the efficiency when there is a decrease in layer thickness from the optimized value [68]. And with the augmentation of thickness the photon absorption falls down because of the recombination of electron hole pair [69]. In this paper, the thickness of $Cs_3Bi_2I_9$ was varied from 400 to 5000 nm for getting optimized thickness for the model. There was change in V_{OC}, J_{SC}, FF and PCE with the variation in absorber layer thickness. These changes have been graphically represented on the **Figure 8**.

Firstly, it has been observed that with the extension of absorber layer thickness, the V_{OC} decreases from 1.4368 to 1.4279 V. The reason behind this is the recombination of charge carrier for their longer travel path. But the J_{SC} has been increased with the increase in absorber layer thickness. This is because of the rise in the spectral response when wavelength is longer. On the contrary the FF get reduced from 84.85% to 72.06% and the reason is the enhancement of series resistance and might be because of the charge carrier recombination along with the resistant losses. The maximum value of PCE was found 20.59% for the thickness of 400 nm which was taken as optimum thickness. For further

Preprints (www.preprints.org) | NOT PEER-REVIEWED | Posted: 25 May 2023 doi:10.20944/preprints202305.1729.v1

augmentation of thickness there was drop in PCE. This is because of the charge pathway resistance and enhanced radiative recombination [70].

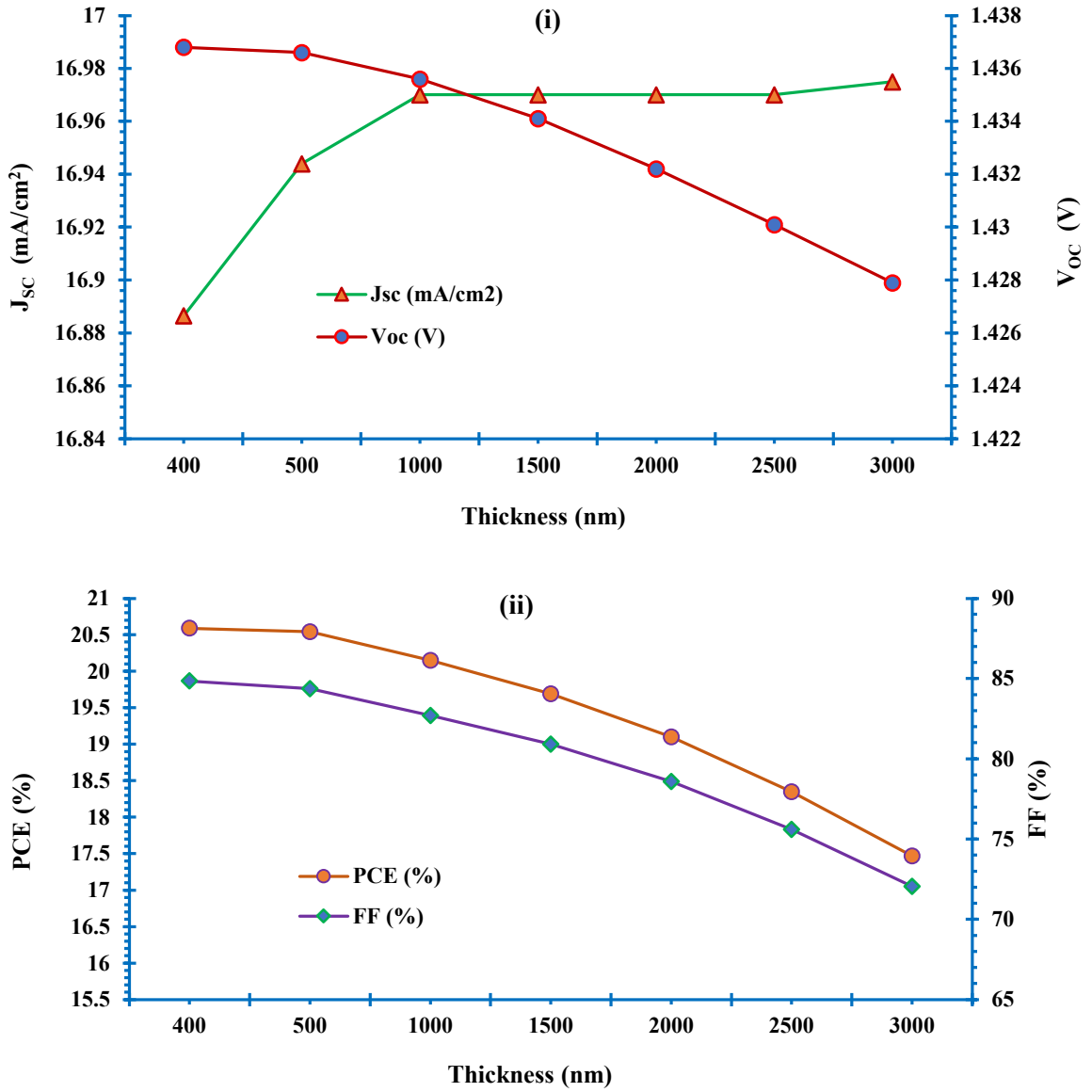

Figure 8: Effect of absorber layer thickness on PSC device' performance parameters (i). (J_{sc}, V_{oc}), and (ii) (FF, PCE).

3.3. Effect of absorber layer band gap

The absorber layer band gap is an important parameter for the absorber layer, and it has a major impact on the effectiveness of the PSCs. In this regard, the tunability is the most important property of PSCs. The energy gap of perovskite absorber is tuned from 1.65 eV to 2.34 eV to investigate the performance of the PSC. **Figure 9** reported that the maximum value of V_{OC} 1.4669V is obtained at 2.34 eV, J_{SC} of 22.88 mA/cm² at 1.65 eV, and the maximum PCE and FF of the device were found 20.9% and 88.79%, respectively at 2.1 eV.

The FF and PCE increased from 63.87% to 88.79% and 19.16% to 20.9% with the augmentation of bandgap from 1.65 to 2.1 eV. After there was a decrease in FF and PCE with increase in band gap because of lowering the band gap increases the number of electrons but the problem is the energy of the electrons wasted as heat energy. On the other hand, higher the band gap the generation of electrons drops for some of the photon's higher energy [71]. The optimum value of bandgap was taken 2.1 eV for the maximum PCE of 20.9%.

Preprints (www.preprints.org) | NOT PEER-REVIEWED | Posted: 25 May 2023 doi:10.20944/preprints202305.1729.v1

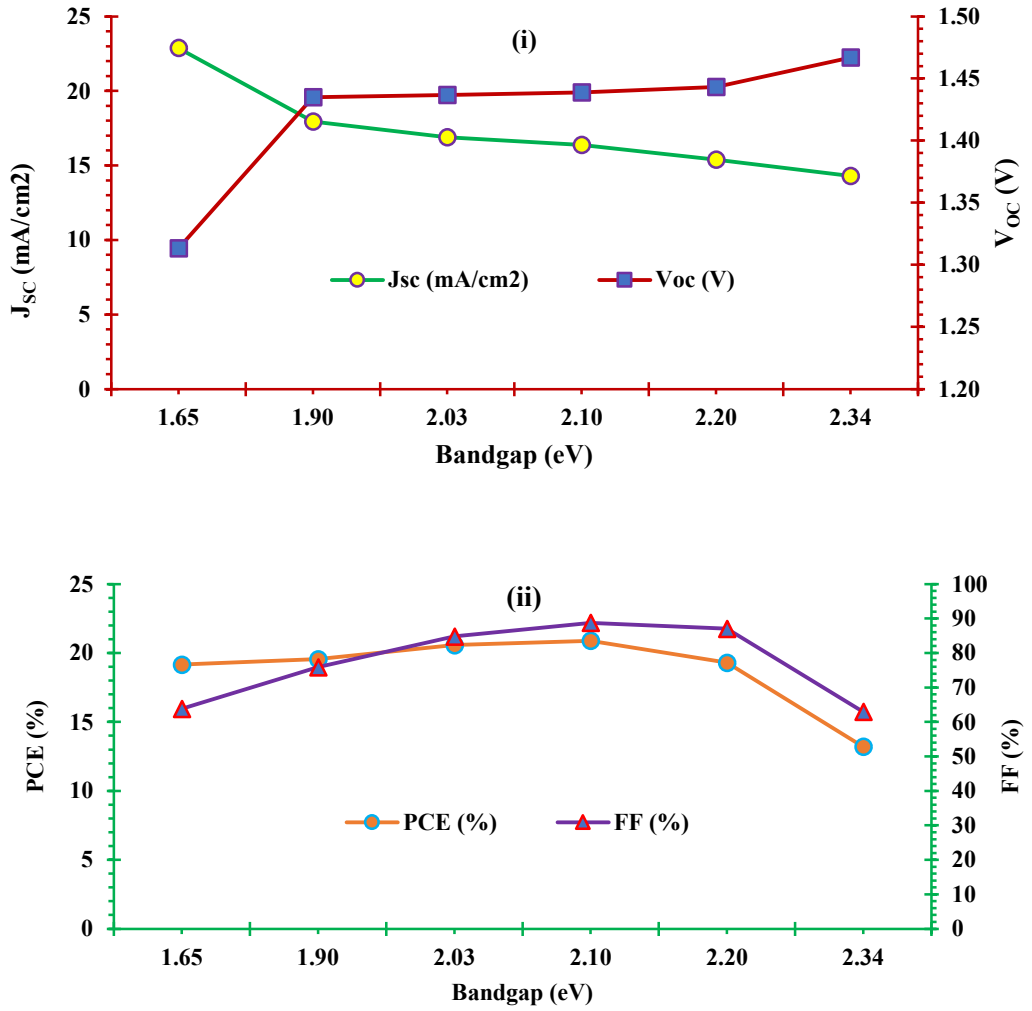

Figure 9: Effect of absorber layer bandgap on (i) Jsc, Voc, and (ii) FF, PCE.

3.4. Effect of absorber layer defect density

In order to attain the stable PV output parameters, the proper amount of defect density is important. The defect density impacts directly on the recombination and generation of electron hole pairs which also has an impact on the efficiency of the PSCs [72]. Defect density depends on the quality of the absorber layer. If the quality is poor, then this causes higher defect density. For this reason, recombination of electron hole pair increases hence reduce the efficiency of the perovskite film.

And this recombination rate depends on the diffusion length, which is affected by the bulk defect density of the PSC. Shockley-Read-Hall (SRH) recombination is the most important type of recombination in PSCs, the calculation of the diffusion length can be done by the trap assisted SRH recombination model [73]. Following two Equations (9 and 10) is used to describe SRH recombination.

$$R_{SRH} = \frac{np - {n_i}^2}{\left[\pi\left(p + n + \frac{2n_i \cosh(E_i - E_t)}{kT}\right)\right]} \quad (9)$$

$$\tau = \frac{1}{[\sigma \times N_t \times V_{th}]} \quad (10)$$

where, τ represents the life time of charge carriers, σ is the capture cross section of charge carriers, N_t is the defect density of the perovskite absorber layer, V_{th} is the thermal velocity of charge carriers.

Preprints (www.preprints.org) | NOT PEER-REVIEWED | Posted: 25 May 2023 doi:10.20944/preprints202305.1729.v1

The diffusion length, $L = \sqrt{D\tau}$, where $D = \frac{kT}{e}\mu$. Here, D refers to the diffusion coefficient and τ refers to the lifetime of minority carriers. In addition to that k denotes as Boltzmann's constant, e refers to the charge of electron, T refers to the temperature, and μ denotes as mobility of charge carrier.

The defect density has an impact on the value of V_{OC} by the following Equation 11.

$$V_{oc} = \frac{kT}{q}\ln\left(\frac{J_{sc}}{J_o} + 1\right) \quad (11)$$

where, J_O and J_{SC} represent the recombination current density and short-circuit current density, respectively.

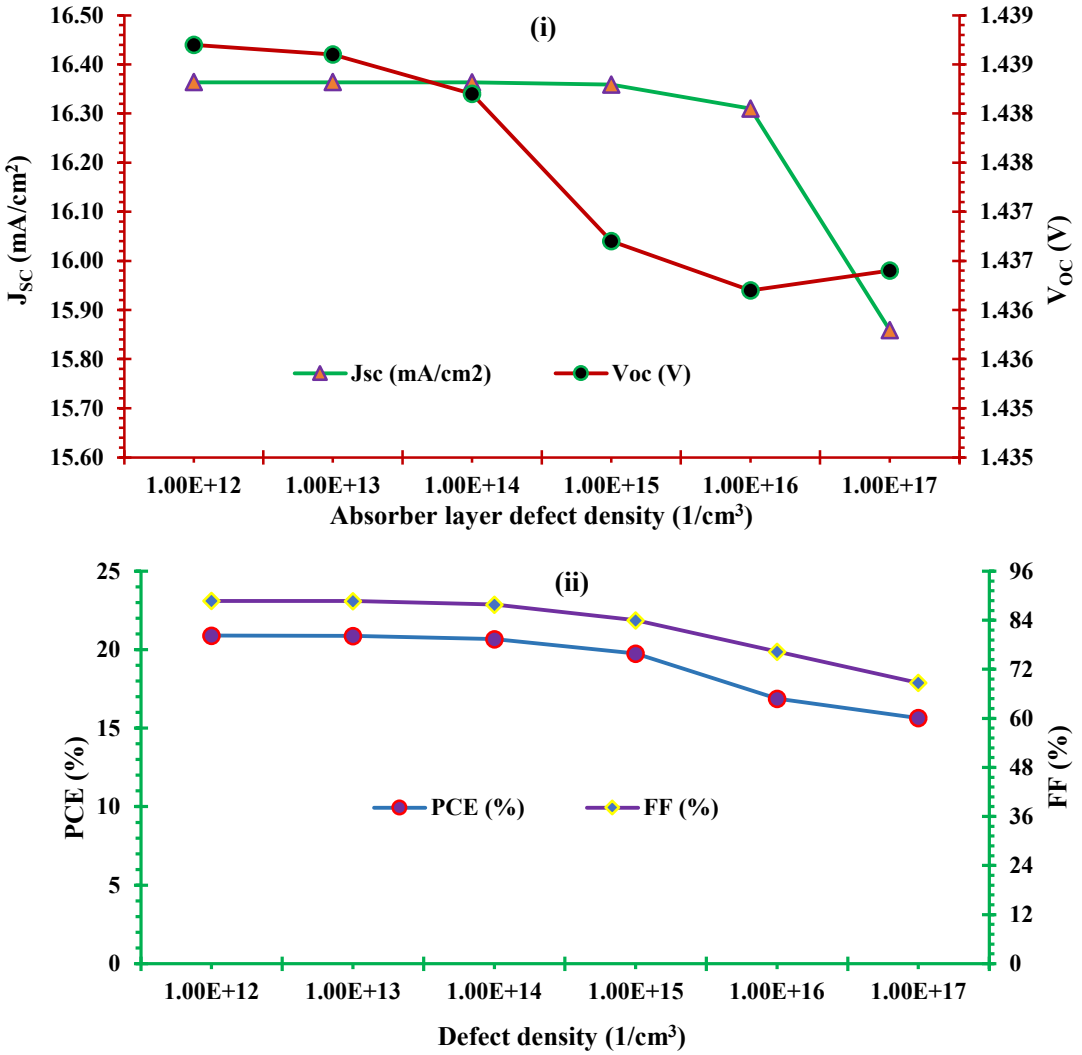

Figure 10: Effect of absorber layer defect density on (i) Jsc, Voc, and (ii) FF, PCE.

In order to get the optimum defect density, N_t of the absorber layer on the PSCs performance is analyzed by taking the values from 10^{12} cm^{-3} to 10^{17} cm^{-3}. **Figure 10** shows with the increase in defect density all the photovoltaic parameters decrease. The V_{OC} drops from 1.4387 V to 1.4364 V and the J_{sc} from 16.364 to 15.859 mA/cm^2. A high density of defects can lead to a decrease in V_{OC} due to the increase in recombination. In devices with high defect densities, the recombination rate becomes dominant, leading to a decrease in V_{OC}. In addition, the increase in defect density can lead to an increase in the trap-assisted recombination rate, which can also reduce the V_{OC} of the device. The values PCE and FF remains almost similar up to the defect density of 10^{12} cm^{-3} to 10^{14} cm^{-3} and reduce

Preprints (www.preprints.org) | NOT PEER-REVIEWED | Posted: 25 May 2023 doi:10.20944/preprints202305.1729.v1

significantly after 10^{15} cm^{-3}. Therefore, the optimal defect density is taken as 10^{12} cm^{-3}. The maximum PCE and FF is found to be 20.9% and 88.79% respectively for the defect density of 10^{-12} cm^{-3}.

3.5. Effect of carrier density

The doping of ETL and HTL can be carried out using one of the two methods. Minority carriers can be used to accomplish the doping rate., however this method dramatically reduces the photovoltaic characteristics. On the other hand, most carriers with greatly improved PV characteristics can also achieve it. PSC performance will be improved with an intermediate level of doping density.

3.5.1. Effect of donor density of ETL

In order to find the best suitable doping concentration of ETL, the donor density for WS_2 was enhanced from 10^{15} cm^{-3} to 10^{19} cm^{-3}. The variation of V_{oc}, J_{sc}, FF and the PCE was shown in **Figure 6**. The PCE and FF increased from 19.88% to 20.96% and 82.53% to 89.03%, respectively with the increase in donor density from 10^{15} to 10^{18} cm^{-3}. The J_{sc} was almost constant with the variation and there was a sudden drop after 10^{18} cm^{-3}. Additionally, the V_{oc} enhanced from 1.43V to 1.44V with the rise in doping concentration. The optimal value of donor density was taken as 10^{18} cm^{-3} as the maximum PCE 20.96% was found at that value. The higher value of N_D makes it easy to extract charge and transportation of charge at the ETL/perovskite interface [74].

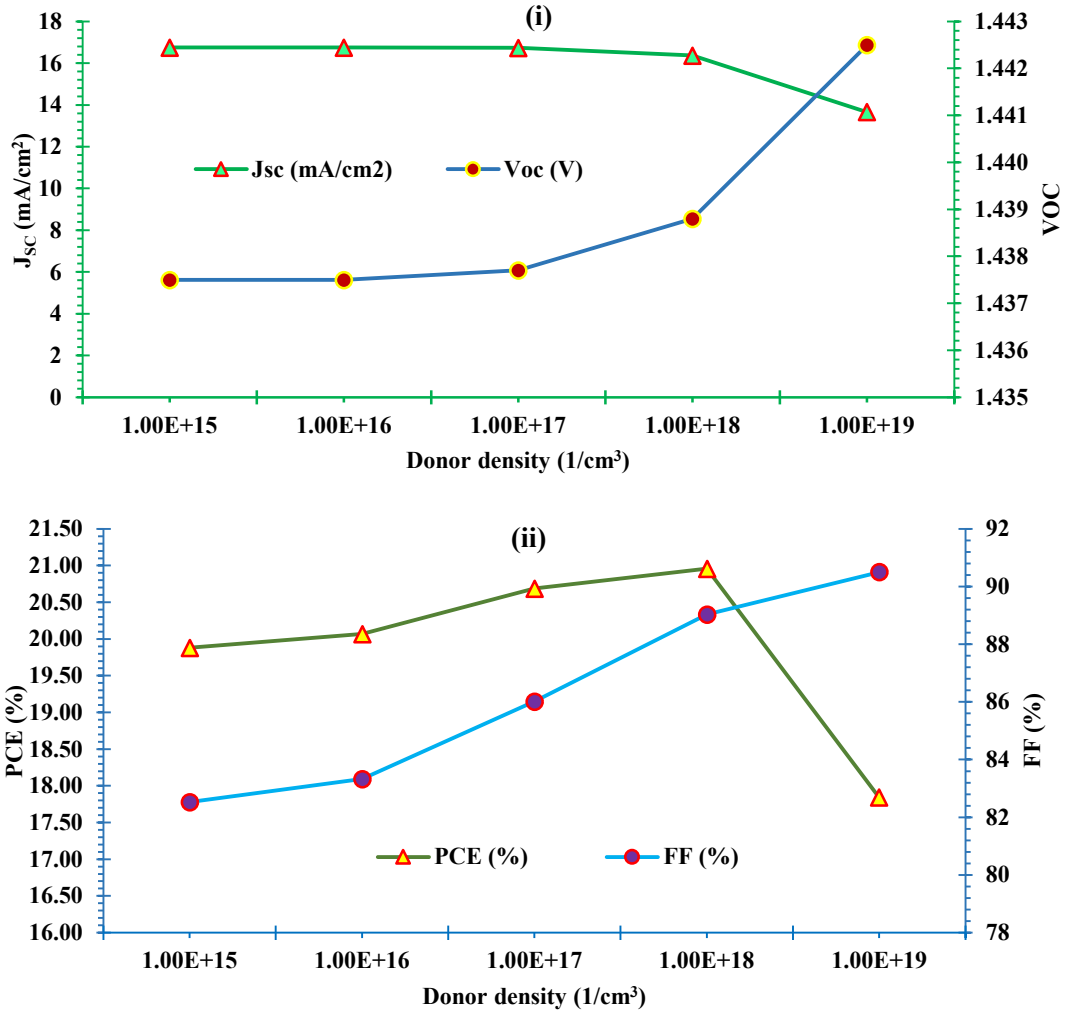

Figure 11: Effect of donor density of ETL (WS_2) on (i) Jsc, Voc, and (ii) FF, PCE.

Preprints (www.preprints.org) | NOT PEER-REVIEWED | Posted: 25 May 2023 doi:10.20944/preprints202305.1729.v1

3.5.2. Effect of acceptor density of HTL

The variation of acceptor density of HTL(N_A) has a major influence on the performance of PSCs. Small amount of variation in acceptor concentration caused variation in the stability of the PSCs. To obtain the optimum value of N_A, the N_A was varied from 10^{16} cm^{-3} to 10^{20} cm^{-3}. There was a small increase in V_{oc} and J_{sc} from 1.4385V to 1.4388V and 16.359 mA/cm² to 16.366 mA/cm² with the increase in HTL acceptor density.

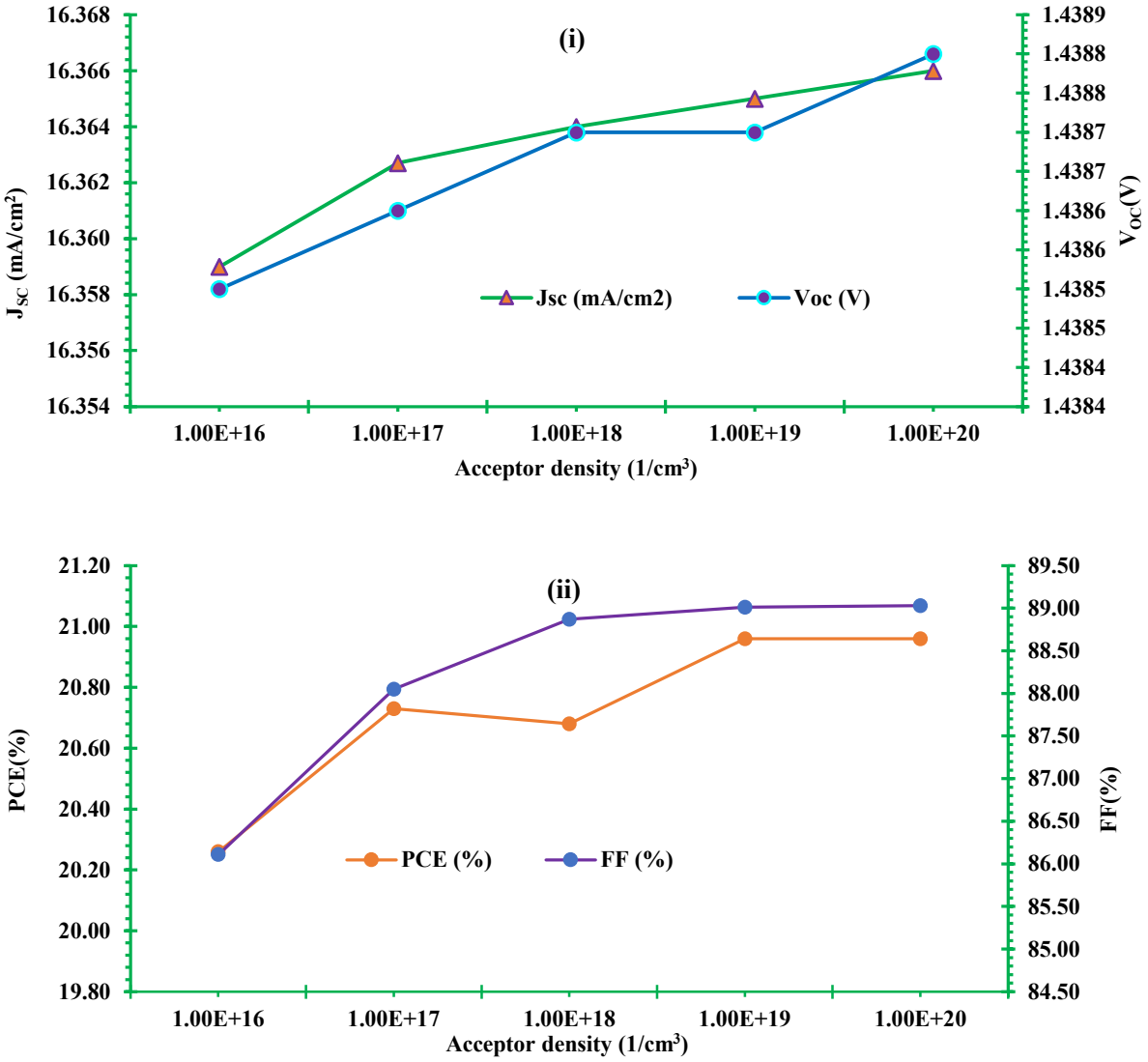

Figure 12: Effect of acceptor density of HTL(NiO) on (i) Jsc, Voc, and (ii) FF, PCE.

In addition to that the PCE and FF was improved from 20.26% to 20.96% and 86.11% to 89.03%, respectively with the augmentation of N_A. Therefore, the optimum value of N_A was taken 10^{20} cm^{-3} as the maximum PCE 20.96% was found at that value of acceptor concentration. The higher the N_A, the production of interface electric field among the PSC layer is higher. It causes the increase in electric potential. However, this growth in PCE brings a higher recombination of charge carriers, which causes an increase in dopant concentration in the absorber layer[74,75].

3.6. Comparison of initial and optimized final model

An improvement of current-voltage characteristic can be seen from **Figure 13** for the optimized final model than the initial model. From the J-V characteristic curve, performance parameters of a

Preprints (www.preprints.org) | NOT PEER-REVIEWED | Posted: 25 May 2023 doi:10.20944/preprints202305.1729.v1

PSC device can be understood. Here, from the J-V curve it can be observed that for the final optimized model an improved I-V curve is obtained than that of initial model.

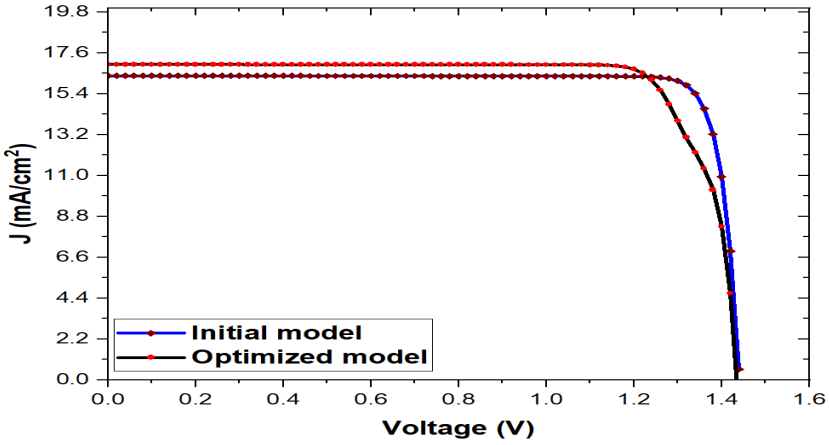

Figure 13: Comparison of J-V characteristic curve of initial and final optimized model.

Figure 14 depicts that the quantum efficiency in optimized final model is higher than the quantum efficiency of initial model. To obtain proper knowledge about quantum efficiency of the initial model and optimized final model, the wavelength was varied from 300 nm to 900 nm. In this wavelength range, the quantum efficiency varied due to tuning of different input attributes such as bandgap and thickness of absorber layer, carrier density and defect density of absorber material.

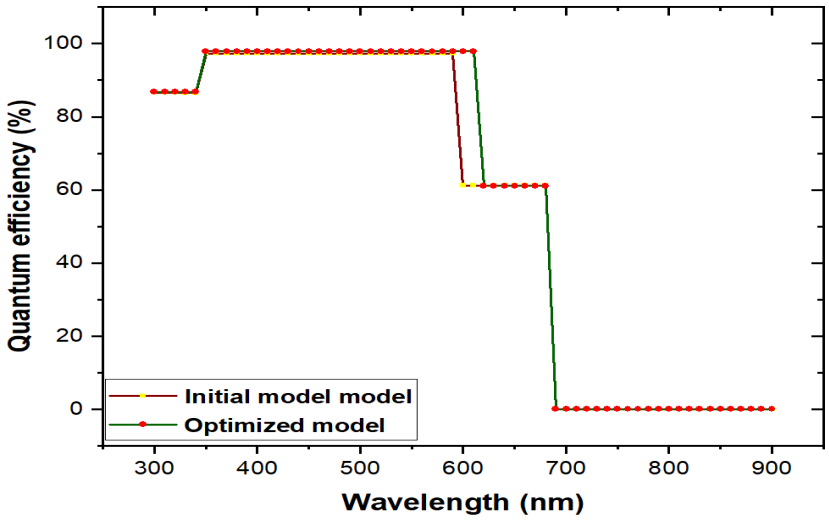

Figure 14: Comparison of capacitance of initial and final optimized model as a function of wavelength.

Quantum efficiency (QE) measures a solar cell's capacity to produce charge carriers from photon energy. From **Figure 14**, it's clear that higher quantum efficiency can be obtained by tuning the PSC device in a proper way, thus higher amount of charge carriers can be produced from the absorber layer, that means generation rate would be increased. As a result, better performance can be obtained due greater generation of electron-hole pairs.

3.7. Comparison with literature

Organic spiro-OMeTAD can be fabricated in flexible and simple method of manufacture, therefore, is the material that is most frequently employed in the commercial and industrial sectors [76]. Despite this, the material is unsuitable for PSCs due to poor hole mobility, low conductivity, high manufacturing costs, and instability brought on by moisture, oxidation, and light. Additionally,

Preprints (www.preprints.org) | NOT PEER-REVIEWED | Posted: 25 May 2023 doi:10.20944/preprints202305.1729.v1

TiO_2 is another popular n-type material which is most commonly used as ETL. Despite having potential for excellent photovoltaic function, photo corrosion resistance, superior thermal stability, and the 3.2eV bandgap presents a difficulty [77]. PSC configurations with these materials and lead-based perovskite shows better characteristics that is clear from table, however due to their toxicity and instability problem further improvement are required through investigating new materials to replace these toxic and instable materials.

Table 5: Comparison of different established model with the present model in this study.

Models	Methods	Voc(V)	Jsc(mA/cm^2)	FF(%)	PCE(%)	Ref
FTO/TiO2/$Cs_3Sb_2I_9$/spiro-OMeTAD/Au	Simulation	1.32	13.13	72.01	12.54	[27]
CZTSe/$MAPbI_3$/$Cd_{1-x}Zn_xS$/FTO	Simulation	1.12	26.45	88.90	27.13	[78]
PTAA/$MAPbI_3$/TiO_2	Experimental	1.11	19.58	76	16.46	[79]
Spiro − OMeTAD/$MAPbI_3$/TiO_2	Simulation	1.27	21.87	79.58	22.13	[80]
Spiro − OMeTAD/$MAPbI_3$/TiO_2	Experimental	1.09	23.83	76.2	19.71	[81]
CuI /$MAPbI_3$/TiO_2	Simulation	1.27	21.89	83.12	23.14	[80]
CuI /$MAPbI_3$/TiO_2	Experimental	0.55	17.8	62	6	[82]
NiO_x/$MAPbI_3$/PCBM : C_{60}/Zr	Experimental	1.08	23.47	79.4	20.13	[83]
FTO/TiO2/Cs3Bi2I9/spiro-MeOTAD/Au	Simulation	1.03	21.02	73.4	11.14	[84]
FTO/TiO_2/$Cs_3Bi_2I_9$/NiO	Simulation	0.92	22.07	68.21	13.82	[84]
ITO/WS_2/$Cs_3Bi_2I_9$/NiO/Au	Simulation	1.438	16.366	89.03	20.96	[Present work]

In this study, a novel PSC model was designed and simulated that shows better performance characteristics after optimization which can be seen from **Table 5Table 5**. Additionally, the selected perovskite material ($Cs_3Bi_2I_9$) is considered much stable [85] which is introduced in the previous section. Therefore, the designed model in this present work can be considered for further experiment and commercialization.

4. Conclusions

In this paper, the modeling and performance analysis was done for the $Cs_3Bi_2I_9$ based PSC using SCAPS-1D. The lead-free $Cs_3Bi_2I_9$ was used as the absorber layer and the selection of this layer was based on the better stability and non-toxicity of this material. WS_2, PCBM, C60, TiO_2, IGZO were used as the ETL material and Cu_2O, CuSCN, $CuSbS_2$, P3HT, PEDOT:PSS, Spiro-OMeTAD, NiO, CuI, CuO was used as the HTL material. Total of 45 different PSC models were simulated with the combination of these HTL and ETL with the $Cs_3Bi_2I_9$ based absorber layer. In addition, Au was taken as the back contact material. After the numerical simulation of these models, the combination of WS_2-$Cs_3Bi_2I_9$-

 doi:10.20944/preprints202305.1729.v1

NiO was found to give the maximum PCE of 20.25%. This combination is the novel model in which WS_2 is used as ETL with $Cs_3Bi_2I_9$ perovskite layer. In order to enhance the performance parameters (V_{OC}, Jsc, FF, PCE) of the PSC and to achieve the maximum PCE, this model was scrutinized by varying the parameters like absorber layer thickness, band gap, defect density and carrier density of the ETL and HTL. The thickness of absorber layer was found to be 400 nm as optimum as PCE was maximum 20.59% at 400 nm. Thin absorber layer was found to give the good efficiency for the perovskite model. There was a significant change in the performance with the variation of absorber layer band gap. For the band gap of 2.1 eV, the PCE was the highest among others. There was found a significant increase in PCE from 20.59% to 20.9% for this bandgap. Though, the defect density has a major impact on the effectiveness of the PSCs, there was observed no such changes in the maximum efficiency with the variation of defect density. The maximum efficiency of 20.9% was found at the absorber layer dopant density of 10^{12} cm^{-3}. There was a gradual increase in the performance parameters with the variation in carrier density. The maximum of 20.96 % PCE was obtained with the ETL donor density of 10^{18} cm^{-3} which was the best we found in our numerical analysis. Since, higher the N_D makes the extraction of the charge easier to the ETL/ perovskite layer. The optimum acceptor density of HTL was found to be 10^{20} cm^{-3} and here also the maximum PCE was found to be 20.96%. Finally, after the full optimization the PSC attained a PCE of 20.96% which was initially found to be 20.25%.

Acknowledgement: Authors are thankful to Prof. M. Burgelman and his co-workers, Department of Electronics and Information Systems, University of Gent, Belgium for supporting with the SCAPS-1D simulation software.

References

1. Fichera A, Samanta S, Datta Peu S, Das A, Sanowar Hossain M, Abdul Mannan Akanda M, et al. A Comprehensive Review on Recent Advancements in Absorption-Based Post Combustion Carbon Capture Technologies to Obtain a Sustainable Energy Sector with Clean Environment. Sustainability 2023, Vol 15, Page 5827 2023;15:5827. https://doi.org/10.3390/SU15075827.
2. Azam W, Khan I, Ali SA. Alternative energy and natural resources in determining environmental sustainability: a look at the role of government final consumption expenditures in France. Environmental Science and Pollution Research 2022;1:1–17. https://doi.org/10.1007/S11356-022-22334-Z/TABLES/6.
3. Tofu DA, Wolka K, Woldeamanuel T. The impact of alternative energy technology investment on environment and food security in northern Ethiopia. Scientific Reports 2022 12:1 2022;12:1–11. https://doi.org/10.1038/s41598-022-14521-2.
4. Das A, Peu SD. A Comprehensive Review on Recent Advancements in Thermochemical Processes for Clean Hydrogen Production to Decarbonize the Energy Sector. Sustainability 2022, Vol 14, Page 11206 2022;14:11206. https://doi.org/10.3390/SU141811206.
5. Das A, Peu SD, Hossain MdS, Akanda MAM, Salah MM, Akanda MMH, et al. Metal Oxide Nanosheet: Synthesis Approaches and Applications in Energy Storage Devices (Batteries, Fuel Cells, and Supercapacitors). Nanomaterials 2023, Vol 13, Page 1066 2023;13:1066. https://doi.org/10.3390/NANO13061066.
6. Zafeiriou E, Sariannidis N, Tsiantikoudis S, Das A, Datta Peu S, Abdul Mannan Akanda M, et al. Peer-to-Peer Energy Trading Pricing Mechanisms: Towards a Comprehensive Analysis of Energy and Network Service Pricing (NSP) Mechanisms to Get Sustainable Enviro-Economical Energy Sector. Energies 2023, Vol 16, Page 2198 2023;16:2198. https://doi.org/10.3390/EN16052198.
7. Ma S, Yuan G, Zhang Y, Yang N, Li Y, Chen Q. Development of encapsulation strategies towards the commercialization of perovskite solar cells. Energy Environ Sci 2022;15:13–55. https://doi.org/10.1039/D1EE02882K.
8. Kim YH, Cho H, Heo JH, Kim TS, Myoung NS, Lee CL, et al. Multicolored Organic/Inorganic Hybrid Perovskite Light-Emitting Diodes. Advanced Materials 2015;27:1248–54. https://doi.org/10.1002/ADMA.201403751.
9. Dou L, Yang YM, You J, Hong Z, Chang WH, Li G, et al. Solution-processed hybrid perovskite photodetectors with high detectivity. Nature Communications 2014 5:1 2014;5:1–6. https://doi.org/10.1038/ncomms6404.
10. Australian manufacturer achieves 32% efficiency for inorganic perovskite solar cell – pv magazine Australia n.d. https://www.pv-magazine-australia.com/2022/10/18/australian-manufacturer-achieves-32-efficiency-for-inorganic-perovskite-solar-cell/ (accessed October 18, 2022).
11. Kojima A, Teshima K, Shirai Y, Miyasaka T. Organometal halide perovskites as visible-light sensitizers for photovoltaic cells. J Am Chem Soc 2009;131:6050–1. https://doi.org/10.1021/JA809598R/SUPPL_FILE/JA809598R_SI_001.PDF.
12. Ameri M, Ghaffarkani M, Ghahrizjani RT, Safari N, Mohajerani E. Phenomenological morphology design of hybrid organic-inorganic perovskite solar cell for high efficiency and less hysteresis. Solar Energy Materials and Solar Cells 2020;205:110251. https://doi.org/10.1016/J.SOLMAT.2019.110251.
13. Xiang T, Zhang Y, Wu H, Li J, Yang L, Wang K, et al. Universal defects elimination for high performance thermally evaporated CsPbBr3 perovskite solar cells. Solar Energy Materials and Solar Cells 2020;206:110317. https://doi.org/10.1016/J.SOLMAT.2019.110317.
14. Bi H, Han G, Guo M, Ding C, Zou H, Shen Q, et al. Multistrategy Preparation of Efficient and Stable Environment-Friendly Lead-Based Perovskite Solar Cells. ACS Appl Mater Interfaces 2022;14:35513–21. https://doi.org/10.1021/ACSAMI.2C06032/SUPPL_FILE/AM2C06032_SI_006.MP4.
15. Shivesh K, Alam I, Kushwaha AK, Kumar M, Singh SV. Investigating the theoretical performance of Cs2TiBr6-based perovskite solar cell with La-doped BaSnO3 and CuSbS2 as the charge transport layers. Int J Energy Res 2022;46:6045–64. https://doi.org/10.1002/ER.7546.
16. Shi Z, Guo J, Chen Y, Li Q, Pan Y, Zhang H, et al. Lead-Free Organic–Inorganic Hybrid Perovskites for Photovoltaic Applications: Recent Advances and Perspectives. Advanced Materials 2017;29:1605005. https://doi.org/10.1002/ADMA.201605005.
17. Ustinova MI, Babenko SD, Luchkin SY, Talalaev FS, Anokhin D v., Olthof S, et al. Experimental evaluation of indium(I) iodide as a lead-free perovskite-inspired material for photovoltaic applications. J Mater Chem C Mater 2022;10:3435–9. https://doi.org/10.1039/D1TC05583F.

18. Romani L, Speltini A, Dibenedetto CN, Listorti A, Ambrosio F, Mosconi E, et al. Experimental Strategy and Mechanistic View to Boost the Photocatalytic Activity of Cs3Bi2Br9 Lead-Free Perovskite Derivative by g-C3N4 Composite Engineering. Adv Funct Mater 2021;31:2104428. https://doi.org/10.1002/ADFM.202104428.
19. Ahmad K, Khan MQ, Khan RA, Kim H. Numerical simulation and fabrication of Pb-free perovskite solar cells (FTO/TiO2/Cs3Bi2I9/spiro-MeOTAD/Au). Opt Mater (Amst) 2022;128:112458. https://doi.org/10.1016/J.OPTMAT.2022.112458.
20. Hamukwaya SL, Hao H, Mashingaidze MM, Zhong T, Tang S, Dong J, et al. Potassium Iodide-Modified Lead-Free Cs3Bi2I9 Perovskites for Enhanced High-Efficiency Solar Cells. Nanomaterials 2022, Vol 12, Page 3751 2022;12:3751. https://doi.org/10.3390/NANO12213751.
21. Koh TM, Krishnamoorthy T, Yantara N, Shi C, Leong WL, Boix PP, et al. Formamidinium tin-based perovskite with low Eg for photovoltaic applications. J Mater Chem A Mater 2015;3:14996–5000. https://doi.org/10.1039/C5TA00190K.
22. Noel NK, Stranks SD, Abate A, Wehrenfennig C, Guarnera S, Haghighirad AA, et al. Lead-free organic–inorganic tin halide perovskites for photovoltaic applications. Energy Environ Sci 2014;7:3061–8. https://doi.org/10.1039/C4EE01076K.
23. Krishnamoorthy T, Ding H, Yan C, Leong WL, Baikie T, Zhang Z, et al. Lead-free germanium iodide perovskite materials for photovoltaic applications. J Mater Chem A Mater 2015;3:23829–32. https://doi.org/10.1039/C5TA05741H.
24. Das A, Peu SD, Akanda MAM, Salah MM, Hossain MS, Das BK. Numerical Simulation and Optimization of Inorganic Lead-Free Cs3Bi2I9-Based Perovskite Photovoltaic Cell: Impact of Various Design Parameters. Energies 2023, Vol 16, Page 2328 2023;16:2328. https://doi.org/10.3390/EN16052328.
25. Lehner AJ, Fabini DH, Evans HA, Hébert CA, Smock SR, Hu J, et al. Crystal and Electronic Structures of Complex Bismuth Iodides A3Bi2I9 (A = K, Rb, Cs) Related to Perovskite: Aiding the Rational Design of Photovoltaics. Chemistry of Materials 2015;27:7137–48. https://doi.org/10.1021/ACS.CHEMMATER.5B03147/SUPPL_FILE/CM5B03147_SI_001.PDF.
26. Park BW, Philippe B, Zhang X, Rensmo H, Boschloo G, Johansson EMJ. Bismuth Based Hybrid Perovskites A3Bi2I9 (A: Methylammonium or Cesium) for Solar Cell Application. Advanced Materials 2015;27:6806–13. https://doi.org/10.1002/ADMA.201501978.
27. Ahmad K, Khan MQ, Kim H. Simulation and fabrication of all-inorganic antimony halide perovskite-like material based Pb-free perovskite solar cells. Opt Mater (Amst) 2022;128:112374. https://doi.org/10.1016/J.OPTMAT.2022.112374.
28. Feng X, Guo Q, Xiu J, Ying Z, Ng KW, Huang L, et al. Close-loop recycling of perovskite solar cells through dissolution-recrystallization of perovskite by butylamine. Cell Rep Phys Sci 2021;2:100341. https://doi.org/10.1016/J.XCRP.2021.100341.
29. Cacovich S, Vidon G, Degani M, Legrand M, Gouda L, Puel JB, et al. Imaging and quantifying non-radiative losses at 23% efficient inverted perovskite solar cells interfaces. Nature Communications 2022 13:1 2022;13:1–9. https://doi.org/10.1038/s41467-022-30426-0.
30. Zheng X, Hou Y, Bao C, Yin J, Yuan F, Huang Z, et al. Managing grains and interfaces via ligand anchoring enables 22.3%-efficiency inverted perovskite solar cells. Nature Energy 2020 5:2 2020;5:131–40. https://doi.org/10.1038/s41560-019-0538-4.
31. Chen M, Ju MG, Garces HF, Carl AD, Ono LK, Hawash Z, et al. Highly stable and efficient all-inorganic lead-free perovskite solar cells with native-oxide passivation. Nature Communications 2019 10:1 2019;10:1–8. https://doi.org/10.1038/s41467-018-07951-y.
32. Tai Q, Guo X, Tang G, You P, Ng TW, Shen D, et al. Antioxidant Grain Passivation for Air-Stable Tin-Based Perovskite Solar Cells. Angewandte Chemie International Edition 2019;58:806–10. https://doi.org/10.1002/ANIE.201811539.
33. Lee S, Kang DW. Highly Efficient and Stable Sn-Rich Perovskite Solar Cells by Introducing Bromine. ACS Appl Mater Interfaces 2017;9:22432–9. https://doi.org/10.1021/ACSAMI.7B04011/SUPPL_FILE/AM7B04011_SI_001.PDF.
34. Fievez M, Singh Rana PJ, Koh TM, Manceau M, Lew JH, Jamaludin NF, et al. Slot-die coated methylammonium-free perovskite solar cells with 18% efficiency. Solar Energy Materials and Solar Cells 2021;230. https://doi.org/10.1016/J.SOLMAT.2021.111189.

35. Wang JTW, Wang Z, Pathak S, Zhang W, Dequilettes DW, Wisnivesky-Rocca-Rivarola F, et al. Efficient perovskite solar cells by metal ion doping. Energy Environ Sci 2016;9:2892–901. https://doi.org/10.1039/C6EE01969B.
36. Bansode U, Naphade R, Game O, Agarkar S, Ogale S. Hybrid perovskite films by a new variant of pulsed excimer laser deposition: A roomerature dry process. Journal of Physical Chemistry C 2015;119:9177–85. https://doi.org/10.1021/ACS.JPCC.5B02561/SUPPL_FILE/JP5B02561_SI_001.PDF.
37. Noel NK, Stranks SD, Abate A, Wehrenfennig C, Guarnera S, Haghighirad AA, et al. Lead-free organic–inorganic tin halide perovskites for photovoltaic applications. Energy Environ Sci 2014;7:3061–8. https://doi.org/10.1039/C4EE01076K.
38. Doroody C, Rahman KS, Kiong TS, Amin N. Optoelectrical impact of alternative window layer composition in CdTe thin film solar cells performance. Solar Energy 2022;233:523–30. https://doi.org/10.1016/J.SOLENER.2022.01.049.
39. Zuo C, Ding L. Solution-Processed Cu2O and CuO as Hole Transport Materials for Efficient Perovskite Solar Cells. Small 2015;11:5528–32. https://doi.org/10.1002/SMLL.201501330.
40. Burgelman M, Nollet P, Degrave S. Modelling polycrystalline semiconductor solar cells. Thin Solid Films 2000;361–362:527–32. https://doi.org/10.1016/S0040-6090(99)00825-1.
41. Burgelman M, Nollet P, Degrave S. Modelling polycrystalline semiconductor solar cells. Thin Solid Films 2000;361–362:527–32. https://doi.org/10.1016/S0040-6090(99)00825-1.
42. Burgelman M, Decock K, Khelifi S, Abass A. Advanced electrical simulation of thin film solar cells. Thin Solid Films 2013;535:296–301. https://doi.org/10.1016/J.TSF.2012.10.032.
43. Xiao Z, Yuan Y, Wang Q, Shao Y, Bai Y, Deng Y, et al. Thin-film semiconductor perspective of organometal trihalide perovskite materials for high-efficiency solar cells. Materials Science and Engineering: R: Reports 2016;101:1–38. https://doi.org/10.1016/J.MSER.2015.12.002.
44. Burgelman M, Verschraegen J, Degrave S, Nollet P. Modeling thin-film PV devices. Progress in Photovoltaics: Research and Applications 2004;12:143–53. https://doi.org/10.1002/PIP.524.
45. Verschraegen J, Burgelman M. Numerical modeling of intra-band tunneling for heterojunction solar cells in scaps. Thin Solid Films 2007;515:6276–9. https://doi.org/10.1016/J.TSF.2006.12.049.
46. Moiz SA, Alahmadi ANM, Aljohani AJ. Design of a Novel Lead-Free Perovskite Solar Cell for 17.83% Efficiency. IEEE Access 2021;9:54254–63. https://doi.org/10.1109/ACCESS.2021.3070112.
47. Sobayel K, Akhtaruzzaman M, Rahman KS, Ferdaous MT, Al-Mutairi ZA, Alharbi HF, et al. A comprehensive defect study of tungsten disulfide (WS2) as electron transport layer in perovskite solar cells by numerical simulation. Results Phys 2019;12:1097–103. https://doi.org/10.1016/J.RINP.2018.12.049.
48. Islam MT, Jani MR, Shorowordi KM, Hoque Z, Gokcek AM, Vattipally V, et al. Numerical simulation studies of Cs3Bi2I9 perovskite solar device with optimal selection of electron and hole transport layers. Optik (Stuttg) 2021;231:166417. https://doi.org/10.1016/J.IJLEO.2021.166417.
49. Lakhdar N, Hima A. Electron transport material effect on performance of perovskite solar cells based on CH3NH3GeI3. Opt Mater (Amst) 2020;99:109517. https://doi.org/10.1016/J.OPTMAT.2019.109517.
50. Wang Y, Xia Z, Liu Y, Zhou H. Simulation of perovskite solar cells with inorganic hole transporting materials. 2015 IEEE 42nd Photovoltaic Specialist Conference, PVSC 2015 2015. https://doi.org/10.1109/PVSC.2015.7355717.
51. Stamate MD. On the dielectric properties of dc magnetron TiO2 thin films. Appl Surf Sci 2003;218:318–23. https://doi.org/10.1016/S0169-4332(03)00624-X.
52. Niemegeers A, Burgelman M. Numerical modelling of ac-characteristics of CdTe and CIS solar cells. Conference Record of the IEEE Photovoltaic Specialists Conference 1996:901–4. https://doi.org/10.1109/PVSC.1996.564274.
53. Husainat A, Ali W, Cofie P, Attia J, Fuller J. Simulation and Analysis of Methylammonium Lead Iodide ($CH_3NH_3PbI_3$) Perovskite Solar Cell with Au Contact Using SCAPS 1D Simulator. Http://WwwSciencepublishinggroupCom 2019;7:33. https://doi.org/10.11648/J.AJOP.20190702.12.
54. Sobayel K, Akhtaruzzaman M, Rahman KS, Ferdaous MT, Al-Mutairi ZA, Alharbi HF, et al. A comprehensive defect study of tungsten disulfide (WS2) as electron transport layer in perovskite solar cells by numerical simulation. Results Phys 2019;12:1097–103. https://doi.org/10.1016/J.RINP.2018.12.049.
55. Wojciechowski K, Leijtens T, Siprova S, Schlueter C, Hörantner MT, Wang JTW, et al. C60 as an efficient n-type compact layer in perovskite solar cells. Journal of Physical Chemistry Letters 2015;6:2399–405. https://doi.org/10.1021/ACS.JPCLETT.5B00902/SUPPL_FILE/JZ5B00902_SI_001.PDF.

56. Islam AM, Islam S, Sobayel K, Emon EI, Jhuma FA, Shahiduzzaman M, et al. Performance analysis of tungsten disulfide (WS2) as an alternative buffer layer for CdTe solar cell through numerical modeling. Opt Mater (Amst) 2021;120:111296. https://doi.org/10.1016/J.OPTMAT.2021.111296.
57. Zuo C, Ding L. Solution-Processed Cu2O and CuO as Hole Transport Materials for Efficient Perovskite Solar Cells. Small 2015;11:5528–32. https://doi.org/10.1002/SMLL.201501330.
58. Raoui Y, Ez-Zahraouy H, Tahiri N, el Bounagui O, Ahmad S, Kazim S. Performance analysis of MAPbI3 based perovskite solar cells employing diverse charge selective contacts: Simulation study. Solar Energy 2019;193:948–55. https://doi.org/10.1016/J.SOLENER.2019.10.009.
59. Kumar MH, Dharani S, Leong WL, Boix PP, Prabhakar RR, Baikie T, et al. Lead-Free Halide Perovskite Solar Cells with High Photocurrents Realized Through Vacancy Modulation. Advanced Materials 2014;26:7122–7. https://doi.org/10.1002/ADMA.201401991.
60. Chen D, Wang Y, Lin Z, Huang J, Chen X, Pan D, et al. Growth strategy and physical properties of the high mobility p-type cui crystal. Cryst Growth Des 2010;10:2057–60. https://doi.org/10.1021/CG100270D/SUPPL_FILE/CG100270D_SI_001.PDF.
61. Hodes G. Perovskite-Based Solar Cells. Science (1979) 2013;342:317–8. https://doi.org/10.1126/SCIENCE.1245473.
62. Liu D, Gangishetty MK, Kelly TL. Effect of CH3NH3PbI3 thickness on device efficiency in planar heterojunction perovskite solar cells. J Mater Chem A Mater 2014;2:19873–81. https://doi.org/10.1039/C4TA02637C.
63. Wu H, Wang LS. A study of nickel monoxide (NiO), nickel dioxide (ONiO), and Ni(O2) complex by anion photoelectron spectroscopy. J Chem Phys 1998;107:16. https://doi.org/10.1063/1.474362.
64. Hock R, Mayer T, Jaegermann W. P-type doping of spiro-MeOTAD with WO 3 and the spiro-MeOTAD/WO 3 interface investigated by synchrotron-induced photoelectron spectroscopy. Journal of Physical Chemistry C 2012;116:18146–54. https://doi.org/10.1021/JP301179V/ASSET/IMAGES/MEDIUM/JP-2012-01179V_0019.GIF.
65. Du(杜会静) H-J, Wang(王韦超) W-C, Zhu(朱键卓) J-Z, Du(杜会静) H-J, Wang(王韦超) W-C, Zhu(朱键卓) J-Z. Device simulation of lead-free CH3NH3SnI3 perovskite solar cells with high efficiency. Chinese Physics B 2016;25:108802–108802. https://doi.org/10.1088/1674-1056/25/10/108802.
66. Anwar F, Mahbub R, Satter SS, Ullah SM. Effect of Different HTM Layers and Electrical Parameters on ZnO Nanorod-Based Lead-Free Perovskite Solar Cell for High-Efficiency Performance. International Journal of Photoenergy 2017;2017. https://doi.org/10.1155/2017/9846310.
67. Ameri M, Mohajerani E, Ghafarkani M, Safari N, Alavi SA. The investigation of the unseen interrelationship of grain size, ionic defects, device physics and performance of perovskite solar cells. J Phys D Appl Phys 2019;52:125501. https://doi.org/10.1088/1361-6463/AAFEA9.
68. Bag A, Radhakrishnan R, Nekovei R, Jeyakumar R. Effect of absorber layer, hole transport layer thicknesses, and its doping density on the performance of perovskite solar cells by device simulation. Solar Energy 2020;196:177–82. https://doi.org/10.1016/J.SOLENER.2019.12.014.
69. Lin L, Jiang L, Li P, Fan B, Qiu Y. A modeled perovskite solar cell structure with a Cu2O hole-transporting layer enabling over 20% efficiency by low-cost low-temperature processing. Journal of Physics and Chemistry of Solids 2019;124:205–11. https://doi.org/10.1016/J.JPCS.2018.09.024.
70. Alam I, Ashraf MA. Effect of different device parameters on tin-based perovskite solar cell coupled with In2S3 electron transport layer and CuSCN and Spiro-OMeTAD alternative hole transport layers for high-efficiency performance. Https://DoiOrg/101080/1556703620201820628 2020. https://doi.org/10.1080/15567036.2020.1820628.
71. Sadanand, Dwivedi DK. Modeling of photovoltaic solar cell based on CuSbS absorber for the enhancement of performance. IEEE Trans Electron Devices 2021;68:1121–8. https://doi.org/10.1109/TED.2020.3048326.
72. He Y, Xu L, Yang C, Guo X, Li S. Design and Numerical Investigation of a Lead-Free Inorganic Layered Double Perovskite Cs4CuSb2Cl12 Nanocrystal Solar Cell by SCAPS-1D. Nanomaterials 2021, Vol 11, Page 2321 2021;11:2321. https://doi.org/10.3390/NANO11092321.
73. Chen Y, Shen H, Altermatt PP. Analysis of recombination losses in screen-printed aluminum-alloyed back surface fields of silicon solar cells by numerical device simulation. Solar Energy Materials and Solar Cells 2014;120:356–62. https://doi.org/10.1016/J.SOLMAT.2013.05.051.
74. Mohandes A, Moradi M, Nadgaran H. Numerical simulation of inorganic Cs2AgBiBr6 as a lead-free perovskite using device simulation SCAPS-1D. Optical and Quantum Electronics 2021 53:6 2021;53:1–22. https://doi.org/10.1007/S11082-021-02959-Z.

75. Salah MM, Abouelatta M, Shaker A, Hassan KM, Saeed A. A comprehensive simulation study of hybrid halide perovskite solar cell with copper oxide as HTM. Semicond Sci Technol 2019;34:115009. https://doi.org/10.1088/1361-6641/AB22E1.
76. Alam I, Mollick R, Ashraf MA. Numerical simulation of Cs2AgBiBr6-based perovskite solar cell with ZnO nanorod and P3HT as the charge transport layers. Physica B Condens Matter 2021;618:413187. https://doi.org/10.1016/J.PHYSB.2021.413187.
77. Ghrib T, AL-Saleem NK, AL-Naghmaish A, Elshekhipy AA, Brini S, Briki K, et al. Annealing effect on the microstructural, optical, electrical, and thermal properties of Cu2O/TiO2/Cu2O/TiO2/Si heterojunction prepared by sol-gel technique. Micro and Nanostructures 2022;164:107119. https://doi.org/10.1016/J.SPMI.2021.107119.
78. Khattak YH, Vega E, Baig F, Soucase BM. Performance investigation of experimentally fabricated lead iodide perovskite solar cell via numerical analysis. Mater Res Bull 2022;151:111802. https://doi.org/10.1016/J.MATERRESBULL.2022.111802.
79. Jeon YJ, Lee S, Kang R, Kim JE, Yeo JS, Lee SH, et al. Planar heterojunction perovskite solar cells with superior reproducibility. Scientific Reports 2014 4:1 2014;4:1–7. https://doi.org/10.1038/srep06953.
80. Azri F, Meftah A, Sengouga N, Meftah A. Electron and hole transport layers optimization by numerical simulation of a perovskite solar cell. Solar Energy 2019;181:372–8. https://doi.org/10.1016/J.SOLENER.2019.02.017.
81. Ahn N, Son DY, Jang IH, Kang SM, Choi M, Park NG. Highly Reproducible Perovskite Solar Cells with Average Efficiency of 18.3% and Best Efficiency of 19.7% Fabricated via Lewis Base Adduct of Lead(II) Iodide. J Am Chem Soc 2015;137:8696–9. https://doi.org/10.1021/JACS.5B04930/SUPPL_FILE/JA5B04930_SI_001.PDF.
82. Christians JA, Fung RCM, Kamat P v. An inorganic hole conductor for Organo-lead halide perovskite solar cells. improved hole conductivity with copper iodide. J Am Chem Soc 2014;136:758–64. https://doi.org/10.1021/JA411014K/SUPPL_FILE/JA411014K_SI_001.PDF.
83. Zhang H, Ren X, Chen X, Mao J, Cheng J, Zhao Y, et al. Improving the stability and performance of perovskite solar cells via off-the-shelf post-device ligand treatment. Energy Environ Sci 2018;11:2253–62. https://doi.org/10.1039/C8EE00580J.
84. Islam MT, Jani MR, Shorowordi KM, Hoque Z, Gokcek AM, Vattipally V, et al. Numerical simulation studies of Cs3Bi2I9 perovskite solar device with optimal selection of electron and hole transport layers. Optik (Stuttg) 2021;231:166417. https://doi.org/10.1016/J.IJLEO.2021.166417.
85. Chaudhary DK, Sharma A, Kumar A, Chauhan U, Bhasker DrHariP, Dhawan DrPK, et al. Solvent Engineering of Cs3bi2i9 Perovskite Films for Lead-Free Flexible Semi-Transparent Perovskite Solar Cell Devices with Enhanced Efficiency. SSRN Electronic Journal 2022. https://doi.org/10.2139/SSRN.4226736.